THE JOURNAL OF PHYSICAL CHEMISTRY C

Article

Cite This: J. Phys. Chem. C 2019, 123, 17555−17565

pubs.acs.org/JPCC

Thermal Phase Transitions in Superlattice Assemblies of Cuboidal $CH_3NH_3PbI_3$ Nanocrystals Followed by Grazing Incidence X-ray Scattering

Yangning Zhang,[†] Cherrelle J. Thomas,[†] Adrien Guillaussier,[†] Detlef-M. Smilgies,[‡] and Brian A. Korgel*[,†]

[†]McKetta Department of Chemical Engineering and Texas Materials Institute, The University of Texas at Austin, Austin, Texas 78712-1062, United States

[‡]Cornell High Energy Synchrotron Source (CHESS), Cornell University, Ithaca, New York 14853, United States

Supporting Information

ABSTRACT: Colloidal nanocrystals of $CH_3NH_3PbI_3$ (MAPI) with the tetragonal crystal structure and cuboidal shape terminated by {110} and {002} facets were assembled into superlattices with cubatic structure and heated under nitrogen while collecting in situ grazing incidence small- and wide-angle X-ray scattering (GISAXS and GIWAXS). The nanocrystals have completed a tetragonal-to-cubic phase transition by 60 °C similar to bulk films. GISAXS shows that the superlattice remains stable until 90 °C. At this temperature, GIWAXS reveals the evolution of PbI_2. In situ photoluminescence shows that PbI_2 begins to form at 75 °C, which is about 10−25 °C lower than in bulk MAPI films. Another difference compared to bulk MAPI is that both hexagonal and rhombohedral phases of PbI_2 are observed as thermal degradation products, when the nanocrystals are heated up to 150 °C.

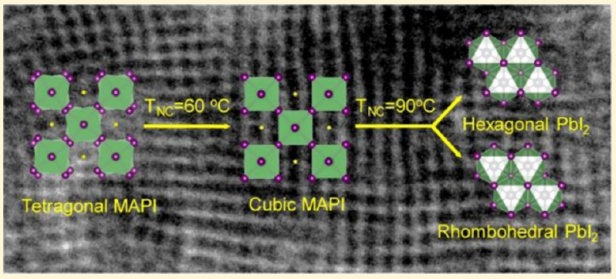

INTRODUCTION

Lead halide perovskites, including hybrid organic−inorganic perovskites (HOIPs), represented by methyl-ammonium lead iodide ($CH_3NH_3PbI_3$, MAPI) are promising materials, especially for solar cells, due to their large optical absorption coefficients, high charge carrier mobility, long carrier diffusion lengths, and high device efficiencies.[1−4] The crystallographic orientation and morphology of the layer can influence device performance, and approaches have been developed to deposit crystallographically oriented MAPI films by manipulating the solvent, reactants and concentrations, and spin-coating procedures.[5−9] Another way to do this would be to assemble nanocrystals with uniform faceted shape into superlattice films with preferred crystallographic orientation, as has been done for a variety of other materials, including metal halide perovskite nanocrystals of $Cs_2AgBiBr_6$, $CH_3NH_3PbBr_3$, and $CsPbBr_3$ with cuboidal shape.[10−27]

Here, we demonstrate the synthesis of uniform MAPI nanocrystals suitable for superlattice assembly by modifying the method of Vybornyi, Yakunin, and Kovalenko[28] with a shorter reaction time and using methyl acetate as an antisolvent for purification. Of the variety of arrested precipitation approaches reported for the synthesis of MAPI nanocrystals,[28−33] some of these have produced nanocrystals with cuboidal shape, but all have had size distributions that have been too broad to make superlattices.[28,31,32] The MAPI nanocrystals produced here have tetragonal crystal phase with cuboidal shape terminated by {110} and {002} crystal facets. These nanocrystals self-assemble into superlattices with cubatic structure and preferred crystallographic orientation.

We then examined the thermal phase stability of MAPI nanocrystal superlattices using in situ grazing incidence small- and wide-angle X-ray scattering (GISAXS and GIWAXS). Phase stability is particularly important for device applications.[34,35] Some lead halide perovskite nanocrystals, such as $CsPbI_3$ and $CsPbI_{3-x}Br_x$, have exhibited differences in phase stability compared to the bulk material, such as a metastable room-temperature cubic phase, and inhibited halide segregation.[36−38] MAPI exhibits three crystal structures: orthorhombic ($T < -111$ °C),[39,40] tetragonal ($-111 < T < 54$ °C),[40,41] and cubic ($T > 54$ °C).[42] One study of MAPI nanoplatelets at low temperature indicated that the tetragonal-to-orthorhombic phase transition occurred at a slightly lower temperature (−123 °C) than in the bulk.[43] We are not aware of any studies examining the tetragonal-to-cubic transition in MAPI nanocrystals. Above 100 °C, MAPI degrades to generate volatile species and PbI_2 by one of these proposed pathways[44−48]

$$CH_3NH_3PbI_3 \rightarrow CH_3I + NH_3 + PbI_2 \quad (1)$$

$$CH_3NH_3PbI_3 \rightarrow CH_3NH_2 + HI + PbI_2 \quad (2)$$

Received: April 6, 2019
Revised: June 8, 2019
Published: June 20, 2019

DOI: 10.1021/acs.jpcc.9b03223
J. Phys. Chem. C 2019, 123, 17555−17565

Previous in situ transmission electron microscopy (TEM) and electron diffraction (ED) studies of MAPI microplates showed the evolution of PbI_2 after heating to 85 °C for 60 s.[49] GISAXS/GIWAXS data and photoluminescence (PL) spectra with in situ heating show that the MAPI nanocrystals change from tetragonal-to-cubic crystal structure at 55−60 °C and begin to degrade at temperatures as low as 75 °C to PbI_2. Upon reaching temperatures as high as 150 °C, the PbI_2 byproduct exhibits both hexagonal and rhombohedral phases. Thermal degradation of MAPI usually proceeds to PbI_2 with the hexagonal crystal structure, and the appearance of the rhombohedral phase of PbI_2 has only been observed in one study in the case of light-induced degradation of bulk MAPI films.[50] GIWAXS data showed that the films exhibited preferred crystal orientations on the substrate throughout the heating process.

EXPERIMENTAL DETAILS

Materials. Lead iodide (Sigma, 99.999% trace metal basis), methyl amine dissolved in tetrahydrofuran (2 M CH_3NH_2 in THF, Sigma), 1-octadecene (ODE) (Sigma, 90%), oleylamine (OAm) (Sigma, 98%, LOT #MKBV1987V), oleic acid (OA) (Sigma, 90%), hexane (Sigma, 95%, anhydrous), toluene (Sigma, 99.8%, anhydrous), chloroform (Sigma, 99%, anhydrous), and methyl acetate (Sigma, 99.5%, anhydrous) were purchased and used as received. TEM grids were continuous carbon-coated 200 mesh copper grids (Electron Microscopy Science, LOT #180307). Silicon wafer substrates (University Wafer) were p-type with 650 μm thickness and <100> orientation.

MAPI Nanocrystal Synthesis. MAPI nanocrystals were prepared according to Vybornyi, Yakunin, and Kovalenko,[28] with minor modifications needed to produce uniform nanocrystals with good dispersibility, which involved rapid quenching of the reaction (after 5 s) and product isolation by antisolvent precipitation with methyl acetate. In a 50 mL three-neck flask, 86 mg (0.187 mmol) of PbI_2 and 5 mL of octadecene were combined and placed under vacuum for 1 h at 120 °C. After blanketing the reaction mixture with nitrogen, 0.3 mL of oleylamine (OAm) and 0.8 mL of oleic acid (OA) were added (both preheated to ∼70 °C). The reaction flask was placed under vacuum again for 30 min at 120 °C. The reaction mixture was blanketed with nitrogen again, the temperature was lowered to 55 °C, and a mixture of 0.18 mL of 2 M methyl amine in THF and 0.8 mL of OA was added. After only 5 s, the flask was immersed in an ice water bath to quench the reaction. The nanocrystals were precipitated by adding methyl acetate (1:1 v/v) followed by centrifugation. After discarding the supernatant, the nanocrystals were redispersed in hexane and centrifuged again to precipitate poorly capped nanocrystals. The supernatant was collected and stored sealed under nitrogen in a freezer. A typical reaction yields ∼70 mg of nanocrystals. Approximately, 30 wt % of the final product is composed of ligand. The molar conversion of reactants to MAPI nanocrystals is about 60%.

Nanocrystal Superlattice Assembly. Superlattices of MAPI nanocrystals were prepared by solvent evaporation on TEM grids for TEM imaging or Si wafer substrates for scanning electron microscopy (SEM), X-ray diffraction (XRD), and GISAXS/GIWAXS using the methods of Guillaussier et al.[51] It was necessary to store the nanocrystals as concentrated dispersions in hexane. The nanocrystals were found to degrade in either chloroform or toluene. Therefore, to form superlattices from one of these other solvents, nanocrystals were first dried in a 3 mL glass vial by evaporating 40 μL of a hexane dispersion, then briefly redispersing the nanocrystals by adding 280 μL of chloroform or toluene, as desired. The substrate was then placed flat on the bottom of the vial, and the solvent was evaporated. Superlattices were allowed to dry overnight at room temperature in an Ar-filled glovebox to ensure complete removal of the excess solvent prior to characterization.

Transmission Electron Microscopy (TEM). TEM was performed on a FEI Tecnai Biotwin TEM operated at a 80 kV accelerating voltage. High-resolution TEM images and selected area electron diffraction (ED) were obtained using a JEOL 2010F TEM operated at 200 kV.

Scanning Electron Microscopy (SEM) and Energy Dispersive X-ray Spectroscopy (EDS). SEM images were acquired with a Zeiss Supra 40 VP SEM at a 3 kV accelerating voltage. Images were collected through the in-lens detector. SEM/EDS elemental mapping was performed on a Hitachi S5500 SEM at a 20 kV accelerating voltage.

X-ray Diffraction (XRD). A Rigaku R-axis Spider diffractometer was used to perform XRD on MAPI nanocrystal superlattices on Si wafer. The X-ray generator was operated at 40 kV and 40 mA and rotated at 5° s^{-1} for 10 min yielding Cu Kα radiation (λ = 1.54 Å). The 2DP and JADE software were used for background subtraction and data processing.

Grazing Incidence Small-Angle and Wide-Angle X-ray Scattering (GISAXS and GIWAXS). GISAXS and GIWAXS were performed at the D1 beam line of the Cornell High Energy Synchrotron Source (CHESS). Data were obtained with monochromatic X-ray radiation of a wavelength of 1.162 Å, and the incident angle of the beam upon the sample was 0.25°. For temperature-dependent in situ measurements, the sample was placed inside a custom-built heating chamber. The chamber was purged with flowing nitrogen during the experiment. The temperature was increased from 25 to 60 °C at a heating rate of 15 °C/min, then 60−90 °C at a rate of 15 °C/min, and finally from 90 to 150 °C at 20 °C/min. The sample temperature was maintained at 60, 90, or 150 °C for 2 min before each GISAXS/GIWAXS measurement. Small-angle scattered photons were collected with a Pilatus 200K detector of 487 × 407 pixels with a pixel size of 172 μm × 172 μm and a sample-to-detector distance of 1285 mm. Wide-angle scattered photons were collected with a FUJI image plate detector of 2500 × 2000 pixels with a pixel size of 100 μm × 100 μm and a sample-to-detector distance of 156 mm. The patterns were calibrated and integrated using the Fit2D software (version: 12_077_i686_WXP). The patterns were indexed with the aid of indexGIXS-2Mx software.[52]

Optical Measurements. Absorbance and photoluminescence (PL) spectra were acquired for MAPI nanocrystals dispersed in hexane. UV−visible absorbance spectra were measured using a Varian Cary Bio (UV−vis) spectrophotometer, and PL emission spectra were collected with a Varian Cary Eclipse Fluorescence spectrometer. Temperature-dependent PL spectra of MAPI nanocrystal superlattices were acquired using a Fluorolog-3 spectrophotometer (Horiba Jobin Yvon) equipped with a home-built air-free thermostat system. PL quantum yield (QY) was estimated using Rhodamine B as a standard.

DOI: 10.1021/acs.jpcc.9b03223
J. Phys. Chem. C 2019, 123, 17555−17565

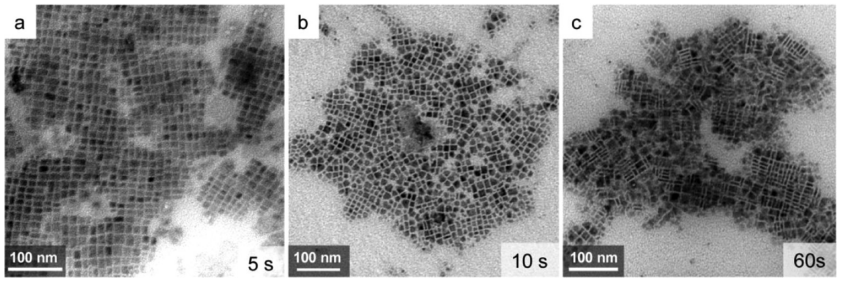

Figure 1. TEM images of $CH_3NH_3PbI_3$ (MAPI) nanocrystals produced using three different reaction times of (a) 5 s, (b) 10 s, and (c) 60 s. The aspect ratio and polydispersity of the cuboidal nanocrystals increase with longer reaction times (see the Supporting Information for accompanying histograms of size and aspect ratio corresponding to these samples.).

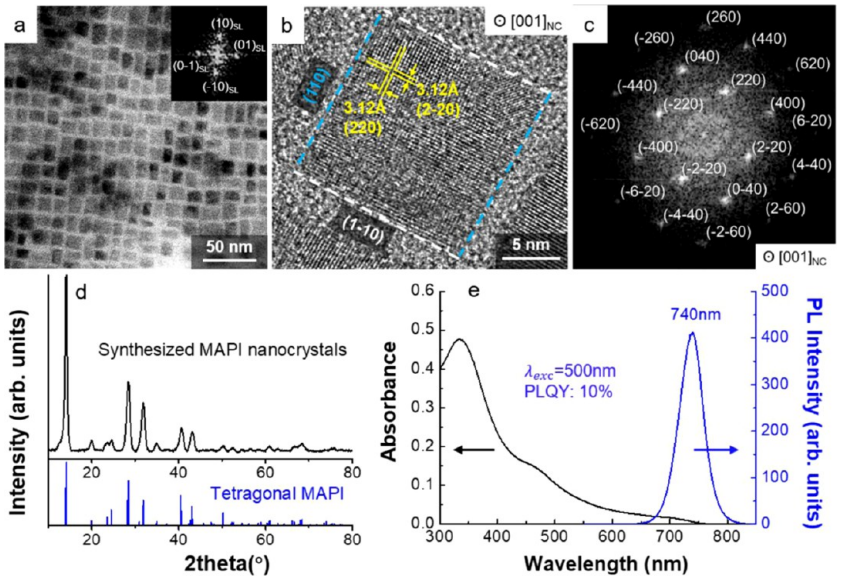

Figure 2. (a, b) TEM images, an (c) FFT of the image in (b), (d) XRD, and (e) room-temperature UV−vis absorbance and PL emission spectra of MAPI nanocrystals used in this study to fabricate superlattices. The nanocrystals have a slightly anisotropic cuboidal shape; the inset in (a) is the FFT of the TEM image indexed to a nanocrystal monolayer with cubatic order; the *g*-values of the four spots are equivalently 0.063 nm^{-1}, corresponding to a *d*-spacing of 15.9 nm. The lattice spacings of 3.12 Å labeled in (b) agree with the (220) and $(2\bar{2}0)$ *d*-spacings of bulk tetragonal MAPI of 3.13 Å.[41] The FFT in (c) is indexed to tetragonal MAPI viewed down the [001] zone axis. The XRD pattern in (d) matches tetragonal MAPI (the blue reference pattern is PDF #01-083-7582). A magnification of the absorbance spectra in (e) near the exciton peak wavelength is provided as the Supporting Information.

RESULTS AND DISCUSSION

MAPI Nanocrystal Synthesis and Characterization of their Cuboidal Shape. MAPI nanocrystals were synthesized using the methods of Vybornyi, Yakunin, and Kovalenko,[28] but with a reduced reaction time and a milder antisolvent, methyl acetate, to precipitate the nanocrystals during the purification step. This synthesis relies on the reaction of methyl amine (CH_3NH_2) with PbI_2, in the presence of oleic acid (OA) and oleylamine (OAm) in octadecene (ODE)

$$2\,CH_3NH_2 + 2\,RCOOH + 3PbI_2 \xrightarrow[OA,OAm,ODE]{55°C,5s} 2CH_3NH_3PbI_3 + Pb(RCOO)_2 \quad (3)$$

PbI_2 provides the Pb^{2+} and I^- needed to make $CH_3NH_3PbI_3$, while also releasing a proton from OA to convert methyl amine to $CH_3NH_3^+$ and resulting in lead oleate ($Pb(RCOO)_2$) as a byproduct. OAm and excess OA serve as ligands that stabilize the nanocrystals. We found that an extremely short reaction time of about 5 s led to the most uniform nanocrystals, and that it was necessary to use methyl acetate as an antisolvent to avoid the degradation of the material during purification. Methyl acetate has also been shown to be effective in isolating other lead halide perovskite nanocrystals as well, such as $CsPbI_3$.[36]

The abbreviated reaction time was essential to obtain nanocrystals sufficiently uniform to generate assemblies that exhibited superlattice diffraction peaks in GISAXS measurements. Figure 1 shows TEM images of MAPI nanocrystals obtained from reactions quenched after 5, 10 s, and 1 min. The nanocrystals are cuboidal in shape and slightly extended in one direction. The longer reaction times led to higher aspect ratios and more polydispersity. The nanocrystals in each assembled monolayer in Figure 1a−c exhibit close-packed structure with local cubatic order. However, the nanocrystals made with longer reaction times were more anisotropic and tetragonal in shape and the random orientation of the nanocrystals in the monolayer, along with the size nonuniformity, prevented longer-range periodic order, especially obvious in Figure 1c. Diffraction peaks were never observed in the small-angle X-ray scattering data from assemblies of MAPI nanocrystals made with the longer reaction times. In contrast, the cubatic order of

DOI: 10.1021/acs.jpcc.9b03223
J. Phys. Chem. C 2019, 123, 17555−17565

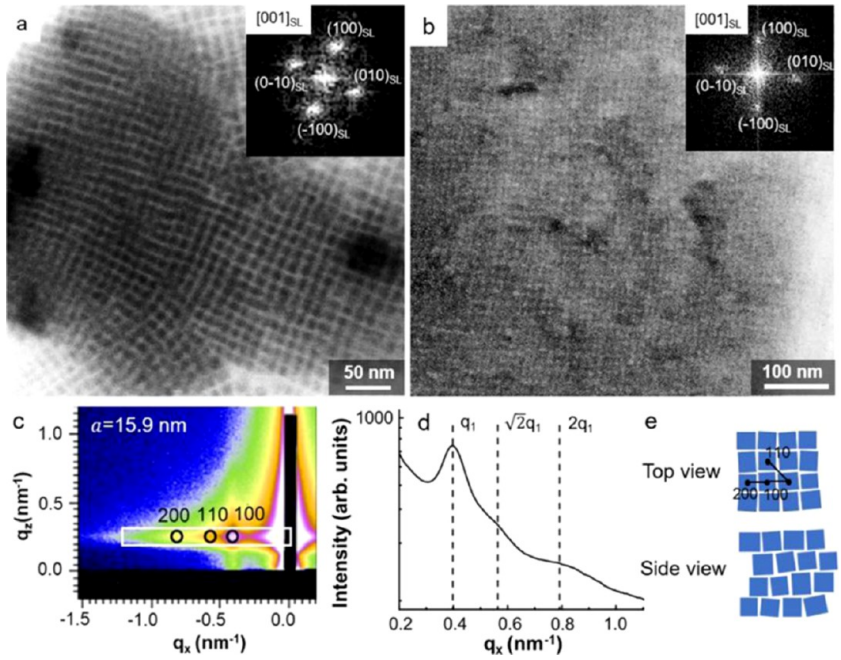

Figure 3. (a) TEM, (b) SEM image, (c) GISAXS, (d) GISAXS horizontal projection, and (e) schematic of MAPI nanocrystal superlattices. In (a), the nanocrystal assembly shows face-to-face contact and 4-fold symmetry in-plane. The inset is the FFT of the TEM image, indexed to [001] zone axis of a square superlattice. The *g*-values of the four spots in FFT are 0.070 nm^{-1} for $(0\bar{1}0)$ and (010) superlattice planes, corresponding to a *d*-spacing of 14.3 nm, and 0.069 nm^{-1} for $(\bar{1}00)$ and (100) superlattice planes, corresponding to a *d*-spacing of 14.4 nm. In (b), the nanocrystals form an island of several hundred nanometers wide and thick. The inset is the FFT of the SEM image, indexed to [001] zone axis of the superlattice. The *g*-values of the four spots in FFT are 0.067 nm^{-1} for $(0\bar{1}0)$ and (010) superlattice planes, corresponding to a *d*-spacing of 14.8 nm, and 0.069 nm^{-1} for $(\bar{1}00)$ and (100) superlattice planes, corresponding to a *d*-spacing of 14.4 nm. The three spots in (c) are (100), (110), and (200) reflections of a cubic superlattice with an average lattice constant of a = 15.9 nm. The peak positions in (d) q/q_1 = 1, $\sqrt{2}$, and 2 are consistent with (100), (110), and (200) reflections. The schematic in (e) shows that the nanocrystal assembly has 4-fold symmetry and periodicity in the plane of the substrate (top view) and broken symmetry and periodicity out-of-plane (side view). The top view labels (100), (110), and (200) indicate the associated *d*-spacings of the superlattice.

assemblies of nanocrystals obtained with the very short 5 s reaction time was much more extended and periodic order is apparent in Figure 1a.

Figure 2a shows another TEM image of MAPI nanocrystals made by quenching the reaction after only 5 s. Again, the nanocrystals exhibit a slight elongation in one crystal direction: the average aspect ratio of these nanocrystals is 1.3 ± 0.3, with average lengths of the long and short edges of 13.4 ± 2.4 and 10.3 ± 1.5 nm, respectively. The nanocrystals have assembled into a monolayer with cubatic order. The long axis of the nanocrystals is randomly orientated in the assembly but does not disrupt the periodicity extends for about 200−300 nm. Strictly speaking, the local order is tetragonal. However, because the long and short axes of the nanocrystals are randomly oriented, the fast Fourier transform (FFT) of the TEM image is symmetric with four spots with an equivalent *g*-value of 0.063 nm^{-1}. This corresponds to an average superlattice constant or interparticle separation of 15.9 nm. Locally, the interparticle separation is not symmetric, and the average short and long interparticle spacings are 14.4 ± 1.5 and 16.6 ± 1.4 nm, respectively (the histograms are provided as the Supporting Information).

Figure 2d,e also shows XRD and optical data for the MAPI nanocrystals in Figure 2a. The nanocrystals exhibit the tetragonal phase of MAPI (*I*4*cm*, $a = b$ = 8.85 Å, c = 12.6 Å, PDF #01-083-7582).[40,41,53−55] The lattice spacing of 3.12 Å indicated in Figure 2b is well-matched to the (220) *d*-spacing in tetragonal MAPI (3.13 Å),[42] and the FFT in Figure 2c indexes to tetragonal MAPI with a [001] zone axis beam orientation. The cuboidal nanocrystal is bounded by (110), $(1\bar{1}0)$, $(\bar{1}10)$, and $(\bar{1}\bar{1}0)$ facets orthogonal to the substrate, and (001) and $(00\bar{1})$ facets oriented parallel to the substrate. Calculations by Tateyama and co-workers[56] have shown that the tetragonal {110} and {001} planes provide the most stable surfaces, because they are flat and nonpolar, consisting of alternating stacks of neutral $[MAI]^0$ and $[PbI_2]^0$ planes. The absorbance spectra exhibit an exciton peak at 705 nm (1.76 eV). The nanocrystals exhibit band edge luminescence with a PL emission peak at 740 nm (1.67 eV) and QY of about 10%. The blue-shift from the bulk band gap of 1.51 eV indicates that the nanocrystals are small enough to exhibit quantum confinement, similar to what was observed by Vybornyi et al.[28] for their ∼10 nm-diameter MAPI nanocrystals.

MAPI Nanocrystal Superlattices. Figure 3c,d shows that GISAXS data for MAPI nanocrystals assembled into the superlattices shown in the TEM and SEM images in Figure 3a,b. The superlattices were formed by evaporating the solvent from concentrated dispersions of nanocrystals in either hexane or chloroform. We found that MAPI nanocrystals dried from toluene did not form superlattices (see the Supporting Information). Most literature reports of MAPI nanocrystals have used toluene as the solvent for their dispersions, so this might explain in part why ordered assemblies of MAPI nanocrystals have not previously been reported.

The nanocrystals imaged in Figure 3a,b are assembled with cubatic order. The FFTs of the images in the insets have spot patterns with 4-fold symmetry. The superlattice *d*-spacings obtained from the FFTs are 14.3 and 14.4 nm, similar to the

DOI: 10.1021/acs.jpcc.9b03223
J. Phys. Chem. C 2019, 123, 17555−17565

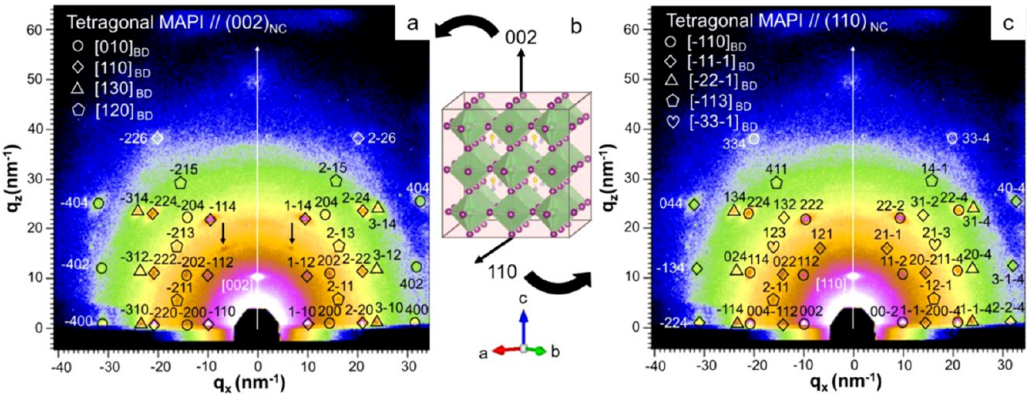

Figure 4. Facets and orientations of MAPI nanocrystals at room temperature: (a), (c) GIWAXS patterns and (b) atomic structure model. (a) and (c) show the same GIWAXS pattern but indexed to two different orientations of the nanocrystals with respect to the substrate. For the subscripts, NC stands for the nanocrystal orientation with respect to the substrate and BD for the beam direction. The spot at $q_x = 0$, $q_z = 10$ nm^{-1} indicates the lattice plane parallel to the substrate (i.e., nanocrystal orientation), whose *d*-spacing matches either (002) or (110) planes of tetragonal MAPI. In (a), the nanocrystal orientation is (002) with respect to the substrate, and the spots are indexed by reflections that occur under at least four beam directions, [010], [110], [130], and [120]. Two extra spots that cannot be indexed by any beam direction are labeled by black arrows. In (c), the nanocrystal orientation is (110) with respect to the substrate, and the spots are indexed by reflections that occur under at least five beam directions, $[\bar{1}10]$, $[11\bar{1}]$, $[\bar{2}2\bar{1}]$, $[\bar{1}13]$, and $[\bar{3}3\bar{1}]$. The spot at $q_x = 0$, $q_z = 50$ nm^{-1} is from the substrate. (b) shows the atomic structure model of a MAPI nanocuboid terminated by (110) and (002) facets of the tetragonal crystal structure. Enlargements of these images are provided as the Supporting Information.

orientationally averaged center-to-center separation of 14.6 ± 1.35 nm between neighboring nanocrystals determined by measuring the positions of the nanocrystals in the images (see the Supporting Information for histograms and additional SEM and TEM images). The horizontal slice of the GISAXS intensity along q_x shown in Figure 3d also shows that GISAXS shows in-plane order. The diffraction features index to a square lattice with a superlattice constant of a_{SL} = 15.9 nm, similar to the monolayer imaged in Figure 2a, but slightly larger than the lattice constants of the thicker assemblies in the TEM and SEM images in Figure 3a,b. There is no out-of-plane order in the GISAXS data in Figure 3c. We propose that the slightly elongated shape and randomly oriented long axes could disrupt the periodic ordering of close-packed planes away from the substrate, as illustrated in Figure 3e. It is also possible that these nanocrystals provide an example of a delocalized vacancy structure.[24,57] Nonetheless, the GIWAXS data, shown in Figure 4, for example, exhibit distinct spot patterns that indicate a strongly preferred crystal orientation in the assembly.

As the analysis of the TEM image in Figure 2b showed, these cuboidal nanocrystals are single crystals of tetragonal MAPI terminated by four {110} facets and two {002} facets. The GIWAXS spot patterns were indexed to determine how the nanocrystals are oriented on the substrate. Figure 4a,c shows the same GIWAXS data indexed based on two different crystallographic orientations. Most spots can be indexed to an (002) orientation, except for the two spots indicated with black arrows. The *d*-spacing corresponding to those spots matches with {211} family, but the angle between these two spots and the (002) spot is not correct. With an orientation of (110), all of the spots can be indexed. This indicates that the nanocrystals definitely exhibit (110) orientation on the substrate, but some coexistence of (002) orientations is also possible and likely. The GIWAXS data further indicate that the cuboidal nanocrystals are terminated with {110} planes, and to have a cuboidal shape with {110} facets, the nanocrystals must also be terminated by two {002} planes, as shown in Figure 4b. Bulk single crystals of MAPI have also been observed with cuboidal shape and {110} and {002} facets,[58,59] and MAPI thin films tend to exhibit {110} surfaces.[55,60−62] It is also worth noting that in high-resolution TEM images of the nanocrystals, it is difficult to distinguish between [002] and [110] orientations, as similar electron diffraction patterns can be indexed by either zone axis (see the Supporting Information for an example).

Simultaneous GISAXS and GIWAXS of Heated MAPI Nanocrystal Superlattices. GISAXS and GIWAXS data were collected simultaneously as superlattices of MAPI nanocrystals were heated from 25 to 150 °C under nitrogen. As shown in Figure 5a, the nanocrystals exhibit the tetragonal crystal structure with strongly preferred (110) and (002) orientations. After heating the superlattice to 60 °C, the crystal structure changes from the tetragonal phase to cubic ($Pm\bar{3}m$) MAPI. As shown in Figure 5d, the $(2\bar{1}1)$, (121), and (123) spots disappear because of the change to cubic symmetry. The tetragonal (110) and (002) orientations become equivalent (001) orientations in the cubic phase. To get a more accurate measure of the phase transition temperature, a superlattice was heated to 45, 55 °C, and then 60 °C (see the Supporting Information for the GIWAXS data). By 60 °C, the tetragonal phase has fully transformed to cubic. At 55 °C, there is still a slight hint of the tetragonal phase. Although a more careful study of the kinetics of this transformation is needed, the tetragonal-to-cubic phase transition temperature of the nanocrystals appears to be slightly higher than 54 °C reported for bulk MAPI.

Once the temperature reaches 90 °C, a new diffraction spot appears next to the (001) spot from cubic MAPI, as shown in Figure 5g. This spot indexes to the (001) spot for hexagonal PbI_2 ($P\bar{3}m1$). The presence of PbI_2 indicates that thermal degradation of MAPI has begun. The evolution of hexagonal PbI_2 also occurs with a (001) crystal orientation on the substrate. This temperature is slightly higher than the onset temperature observed for the degradation of MAPI microplatelets to PbI_2 of 85 °C and lower than 100 °C known for bulk MAPI film.[47,49]

At 150 °C, as shown in Figure 5j, there are new diffraction spots that correspond to rhombohedral PbI_2 ($R\bar{3}m$). The

DOI: 10.1021/acs.jpcc.9b03223
J. Phys. Chem. C 2019, 123, 17555−17565

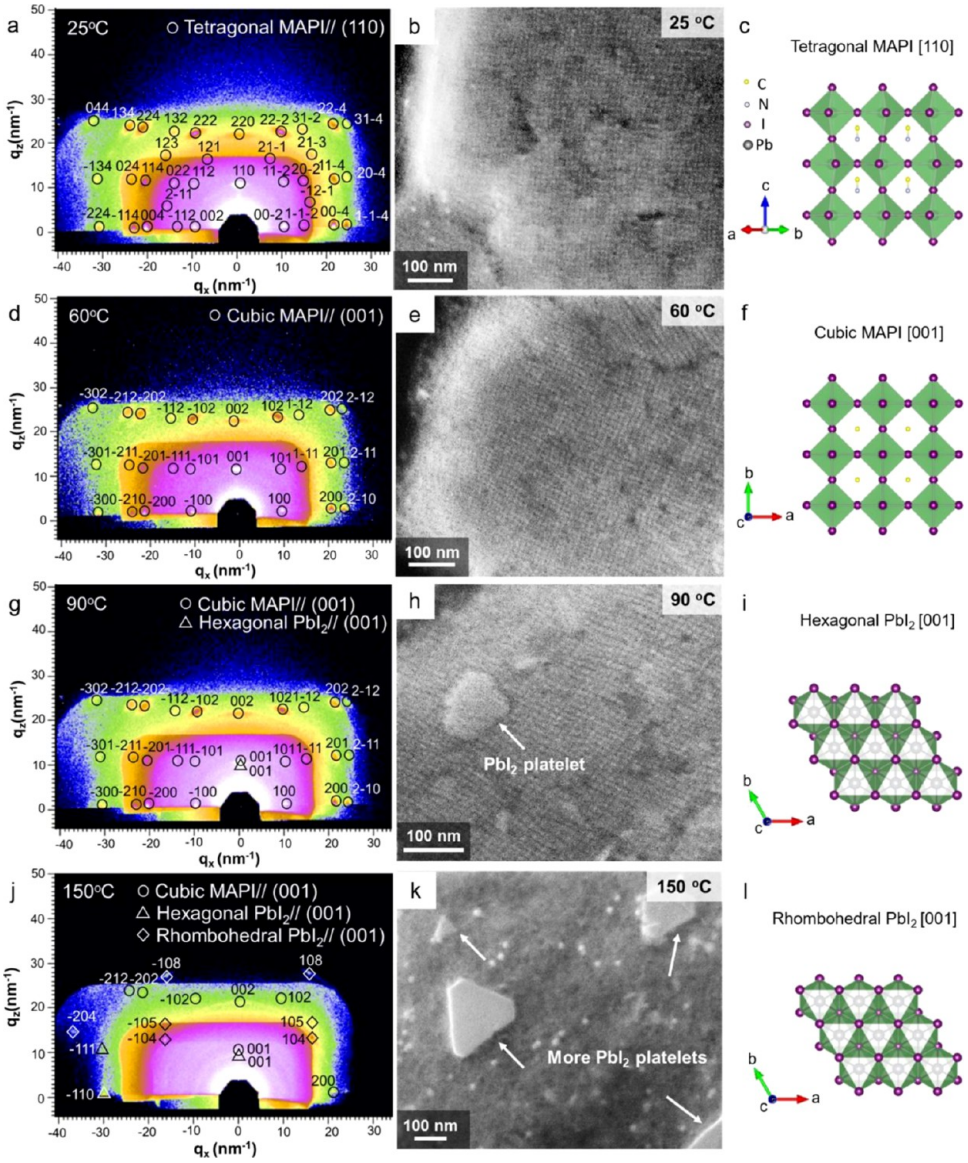

Figure 5. (a, d, g, j) GIWAXS, (b, e, h, k) SEM, and (c, f, i, l) atomic structure models of MAPI nanocrystals from 25 to 150 °C under nitrogen. GIWAXS data were acquired in situ at (a) 25 °C, (d) 60 °C, (g) 90 °C, and (j) 150 °C. The attenuation of the X-ray beam was due to the chamber. The indexation here does not distinguish between the spots from different beam directions to simplify. The GIWAXS pattern in (a) is indexed to tetragonal MAPI with (110) orientation with respect to the substrate (it can also be indexed with (002) orientation). SEM image in (b) shows the morphology of MAPI nanocrystal superlattices. At 60 °C, the GIWAXS pattern in (d) is indexed to cubic MAPI with (001) orientation. The $(2\bar{1}1)$, (121), and (123) spots that showed up in (a) disappeared in (d) due to tetragonal-to-cubic transition. The SEM image in (e) shows that the nanocrystal superlattices are still intact. At 90 °C, the GIWAXS pattern in (g) is indexed to cubic MAPI and hexagonal PbI_2, both with (001) orientation. SEM image in (h) shows that PbI_2 platelets precipitate out of the nanocrystal superlattices. At 150 °C, the GIWAXS pattern in (j) is indexed to cubic MAPI, hexagonal PbI_2, and rhombohedral PbI_2, all with (001) orientation. SEM image in (h) shows that more PbI_2 platelets are formed, whereas MAPI nanocrystals fuse. The atomic structure models in (c), (f), (i), and (l) are tetragonal MAPI viewed from [110] orientation, cubic MAPI from [001] orientation, hexagonal PbI_2 from [001] orientation, and rhombohedral PbI_2 from [001] orientation, respectively (see the Supporting Information for a summary of the crystallographic data used to index the patterns (Table S1) and enlargements of the GIWAXS figures in Figures S10−S13).

newly formed rhombohedral PbI_2 also has a (001) crystal orientation on the substrate. These spots are present along with the diffraction spots from hexagonal PbI_2 and remaining MAPI.

Figure 5 also shows SEM images of the MAPI nanocrystal superlattices before and after heating to 60, 90, and 150 °C. The images in Figure 5b,e are similar, showing that the superlattice structure is maintained after heating to 60 °C. The phase transition of MAPI from its tetragonal phase to the cubic phase does not affect the structure of the superlattice. This is also consistent with GISAXS of the superlattice. As shown in Figure 6a, the q_x projection of in situ GISAXS data still shows the small-angle diffraction peaks from the nanocrystal superlattice after heating to 60 °C corresponding to the cubatic order in the assembly. The peaks are slightly broadened but clearly present.

In Figure 5h, the SEM image shows that relatively large PbI_2 platelets have precipitated from the nanocrystal superlattice after heating to 90 °C. The MAPI nanocrystal superlattice coexists in the background with these large PbI_2 crystallites. The

DOI: 10.1021/acs.jpcc.9b03223
J. Phys. Chem. C 2019, 123, 17555−17565

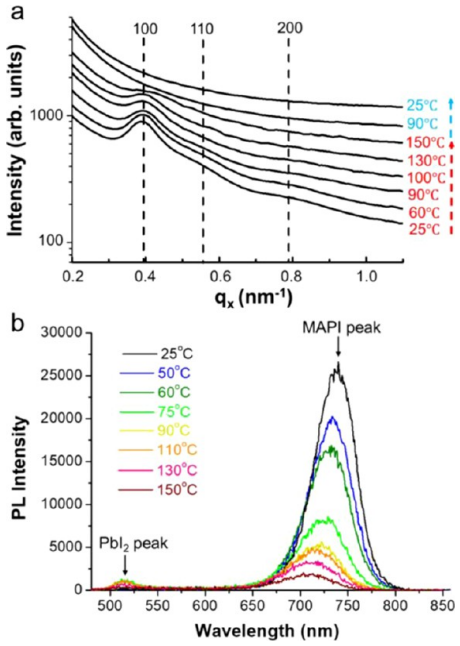

Figure 6. (a) Projection along q_x of in situ GISAXS from a MAPI nanocrystal superlattice heated to 150 °C and then cooled back to room temperature. The diffraction peaks are indexed to (100), (110), and (200) reflections of a cubic superlattice. (b) PL emission spectra (λ_{exc} = 442 nm) from a MAPI nanocrystal superlattice on a silicon wafer in an air-free thermostat system heated from 25 to 150 °C.

GISAXS data in Figure 6a also show the persistence of the superlattice diffraction peaks at this temperature. Computer simulations in the literature have indicated that PbI_2 nucleates and crystallizes from MAPI before any other decomposition products form.[63,64] La Magna and co-workers observed by XRD that MAPI heated to 100 °C undergoes its phase transition from tetragonal-to-cubic before degrading into PbI_2.[65] SEM of the superlattice after heating to 150 °C, in Figure 5k, shows that MAPI nanocrystals have fused under the PbI_2 platelets. The GISAXS data in Figure 6a show that the superlattice order has disappeared by 150 °C. Figure 5c,f,i,l shows atomic structure models for the predominant phase at each temperature of MAPI and PbI_2 in the appropriate crystallographic orientations determined from the GIWAXS data.

The PL spectra of a MAPI nanocrystal superlattice as it was heated are shown in Figure 6b. The intensity of the MAPI PL peak decreases continuously with increasing temperature. The emission peak also shifts to higher energy. This blue-shift of MAPI PL and drop in intensity with increasing temperature, the lack of any abrupt change in PL when the nanocrystals change from tetragonal-to-cubic crystal structure around 60 °C are consistent with the recent work by Diroll et al.[66] At 75 °C, an additional PL peak appears at 513 nm (2.4 eV), which we assign to PbI_2.[67]

Observation of Hexagonal and Rhombohedral PbI_2 as Degradation Products. In all published reports that we are aware of, the PbI_2 degradation product observed after MAPI heating has exhibited the hexagonal crystal structure.[48,49,63,65] There is one report of light-induced degradation of MAPI leading to the rhombohedral phase of PbI_2.[50] The hexagonal and rhombohedral phases of PbI_2 are sometimes referred to as 2H and 12R phases, the 2H phase is stable at room temperature, whereas the 12R phase is stable at high temperature.[68] The 2H-to-12R transition temperature has been reported for bulk PbI_2 to be either 94 or 150 °C.[69,70]

Figure 7 shows TEM images and ED patterns for the degradation products of hexagonal and rhombohedral PbI_2 observed after heating MAPI nanocrystal superlattices to 90 and 150 °C. Figure 7a,b shows that hexagonal platelets have crystallized out of the MAPI nanocrystal superlattice, similar to the SEM image in Figure 5h. In Figure 7c, there are three different particle shapes: a hexagonal platelet, a hexagonal platelet with rounded edges, and a round particle without any facets. The hexagonal platelet looks similar to the hexagonal microplatelets of hexagonal-phase PbI_2 synthesized by solvothermal methods.[71] High-resolution TEM imaging and ED show that the rounded and hexagonal-shaped particles are composed of rhombohedral and hexagonal PbI_2, respectively. Figure 7d–f shows TEM and ED data for a hexagonal platelet. The lattice spacing of 3.95 Å in Figure 7e matches the $(1\bar{1}0)$ lattice plane of hexagonal PbI_2, and the ED pattern in Figure 7f indexes to hexagonal PbI_2 observed down the [001] zone axis. Figure 7g–i shows TEM and ED data for a round particle. The lattice spacing of 2.27 Å in Figure 7h in the high-resolution TEM image corresponds to the (110) *d*-spacing of rhombohedral PbI_2. The ED pattern in Figure 7i from this particle also indexes to a single-crystal domain of rhombohedral PbI_2 observed down the [001] zone axis. We believe that the particle with hexagonal facets and rounded corners is undergoing a hexagonal to rhombohedral phase transition. Further study is needed to understand if there is a unique relationship between these two phases of PbI_2 and the nanoscale structure of MAPI nanocrystals.

CONCLUSIONS

Luminescent nanocrystals of tetragonal phase MAPI were synthesized with cuboidal shape, terminated by four {110} and two {002} facets. The nanocrystals were sufficiently uniform to assemble into superlattices with cubatic structure. The nanocrystals were slightly anisotropic with aspect ratios of about 1.3, which leads to tetragonal packing on a local length scale; yet, because the long and short axes are randomly oriented throughout the superlattice, the interparticle separation determined by GISAXS and FFTs of TEM and SEM images is spatially averaged, and the superlattice structure appears as simple cubic. GIWAXS shows that the superlattices exhibit strongly preferred (110) and (002) crystallographic orientations of MAPI on the substrate. The thermal stability of MAPI nanocrystals was then investigated using GISAXS and GIWAXS with in situ heating. The thermally induced phase transitions and degradation observed by GIWAXS and in situ PL can be summarized as (1) a change in the MAPI crystal structure from tetragonal-to-cubic at 55–60 °C followed by degradation of MAPI to (2) hexagonal PbI_2 beginning at ∼75 °C and then (3) to rhombohedral PbI_2 by ∼150 °C. The tetragonal-to-cubic phase transition occurs at a similar temperature as bulk films. The observed degradation of MAPI nanocrystals to hexagonal-phase PbI_2 at 75 °C indicates that the nanocrystals are chemically less stable than bulk MAPI films, which degrade at about 100 °C. Nonetheless, the superlattice structure is maintained to higher temperatures and co-exists with the crystallizing PbI_2 platelets. Eventually, at 150 °C, the nanocrystals sinter, and rhombohedral PbI_2 is observed. The appearance of rhombohedral PbI_2 in the thermal degradation of MAPI is unusual and perhaps results from a size-related pathway of MAPI nanocrystal decom-

DOI: 10.1021/acs.jpcc.9b03223
J. Phys. Chem. C 2019, 123, 17555–17565

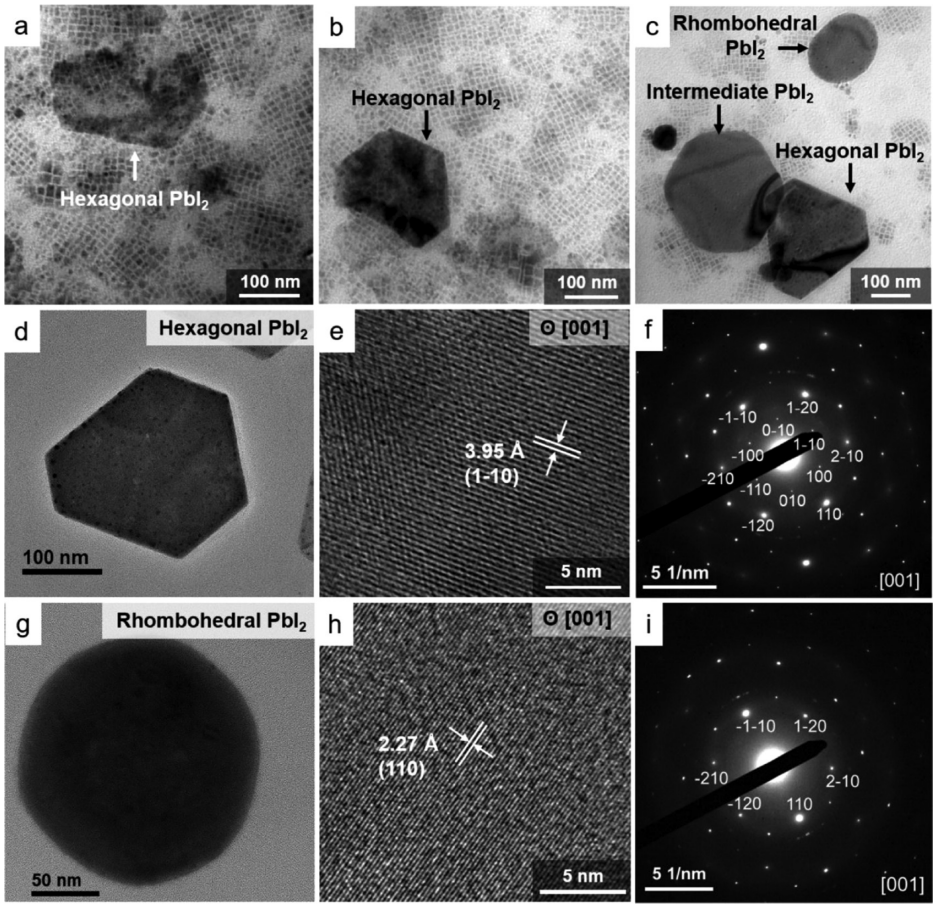

Figure 7. Two phases of PbI_2 evolve as the MAPI nanocrystal superlattices degrade upon heating. (a–c) TEM images are taken from different locations on the same grid of MAPI nanocrystal superlattices heated to 90 °C. (d) Low-magnification TEM image, (e) high-magnification TEM image, and (f) ED pattern on a hexagonal PbI_2 crystal formed by heating MAPI nanocrystal superlattices to 150 °C. (g) Low-magnification TEM image, (h) high-magnification TEM image, and (i) ED pattern on a rhombohedral PbI_2 crystal formed by heating MAPI nanocrystal superlattices to 150 °C. (a) and (b) show the precipitation of PbI_2 out of MAPI nanocrystal superlattices. The hexagonal to rounded shape transformation corresponding to PbI_2 hexagonal to rhombohedral phase transition is shown in (c). Intermediate PbI_2 is the transition state between the two phases. The lattice spacing labeled in (e) is 3.95 Å, which corresponds to $(1\bar{1}0)$ plane of hexagonal PbI_2. The ED pattern in (f) is indexed to hexagonal PbI_2 from [001] zone axis. The lattice spacing labeled in (h) is 2.27 Å, which corresponds to (110) plane of rhombohedral PbI_2. The ED pattern in (i) is indexed to rhombohedral PbI_2 from [001] zone axis (see the Supporting Information for additional SEM images and EDS elemental maps of the hexagonal and rhombohedral particles.).

position. Preferred crystallographic orientations of MAPI and PbI_2 are observed throughout the degradation process. In the case of MAPI, nanocrystals do not appear to offer any significant difference in phase stability compared to the bulk material, but if methods could be developed to sinter the nanocrystals without degradation, this could provide an effective route to obtain lead halide perovskite films with specific crystallographic orientations on a substrate.

■ ASSOCIATED CONTENT

Supporting Information

The Supporting Information is available free of charge on the ACS Publications website at DOI: 10.1021/acs.jpcc.9b03223.

Crystallographic information of tetragonal MAPI, cubic MAPI, hexagonal PbI_2, and rhombohedral PbI_2; TEM images of MAPI NCs synthesized by different reaction times; distribution of center-to-center separation of MAPI nanocrystals in the superlattice determined from TEM; enlarged absorbance spectrum; SEM and TEM images of MAPI nanocrystal superlattices dried from chloroform at room temperature; GISAXS of MAPI nanocrystal amorphous assemblies dried from toluene; enlarged GIWAXS of MAPI nanocrystals at room temperature; high-resolution transmission electron microscopy and ED of MAPI nanocrystals; enlarged GIWAXS of MAPI nanocrystals at different temperatures in the heating chamber; GIWAXS data from the MAPI nanocrystal superlattices cooled back to 25 °C after being heated to 150 °C; GIWAXS of a MAPI nanocrystal superlattice heated to 25, 45, 55, and 60 °C; SEM image and SEM/EDS mappings of degradation products (PDF)

■ AUTHOR INFORMATION

Corresponding Author

*E-mail: korgel@che.utexas.edu. Tel: +1-512-471-5633. Fax: +1-512-471-7060.

ORCID

Detlef-M. Smilgies: 0000-0001-9351-581X

Brian A. Korgel: 0000-0001-6242-7526

DOI: 10.1021/acs.jpcc.9b03223
J. Phys. Chem. C 2019, 123, 17555–17565

Notes

The authors declare no competing financial interest.

■ ACKNOWLEDGMENTS

Financial support of this work was provided by the Robert A. Welch Foundation (F-1464), the Industry/University Cooperative Research Center on Next Generation Photovoltaics (IIP-1540028), and the Center for Dynamics and Control of Materials (CDCM) Materials Research Science and Engineering Center (MRSEC) (DMR-1720595). The Cornell High Energy Synchrotron Source (CHESS) is a national user facility supported by the National Science Foundation under award DMR-1332208. We thank Tushti Shah and Timothy D. Siegler for helpful discussions about interpreting the diffraction patterns. We also thank Kristofer Ohlinger and Raluca Gearba for their assistance with the temperature-dependent PL measurements and Karalee Jarvis for assistance with high-resolution TEM.

■ REFERENCES

(1) Kovalenko, M. V.; Protesescu, L.; Bodnarchuk, M. I. Properties and Potential Optoelectronic Applications of Lead Halide Perovskite Nanocrystals. *Science* **2017**, *358*, 745−750.
(2) Saparov, B.; Mizti, D. B. Organic-Inorganic Perovskites: Structural Versatility for Functional Materials Design. *Chem. Rev.* **2016**, *116*, 4558−4596.
(3) Lee, J.-W.; Hsieh, Y.-T.; De Marco, N.; Bae, S.-H.; Han, Q.; Yang, Y. Halide Perovskites for Tandem Solar Cells. *J. Phys. Chem. Lett.* **2017**, *8*, 1999−2011.
(4) Herz, L. M. Charge-Carrier Dynamics in Organic-Inorganic Metal Halide Perovskites. *Annu. Rev. Phys. Chem.* **2016**, *67*, 65−89.
(5) Saliba, M.; Tan, K. W.; Sai, H.; Moore, D. T.; Scott, T.; Zhang, W.; Estroff, L. A.; Wiesner, U.; Snaith, H. J. Influence of Thermal Processing Protocol upon the Crystallization and Photovoltaic Performance of Organic-Inorganic Lead Trihalide Perovskites. *J. Phys. Chem. C* **2014**, *118*, 17171−17177.
(6) Moore, D. T.; Sai, H.; Tan, K. W.; Smilgies, D.-M.; Zhang, W.; Snaith, H. J.; et al. Crystallization Kinetics of Organic-Inorganic Trihalide Perovskites and the Role of the Lead Anion in Crystal Growth. *J. Am. Chem. Soc.* **2015**, *137*, 2350−2358.
(7) Im, J.-H.; Jang, I.-H.; Pellet, N.; Gratzel, M.; Park, N.-G. Growth of $CH_3NH_3PbI_3$ Cuboids with Controlled Size for High-Efficiency Perovskite Solar Cells. *Nat. Nanotechnol.* **2014**, *9*, 927−932.
(8) Cao, X.; Zhi, L.; Jia, Y.; Li, Y.; Zhao, K.; Cui, X.; Ci, L.; Zhuang, D.; Wei, J. A Review of the Role of Solvents in Formation of High-Quality Solution-Processed Perovskite Films. *ACS Appl. Mater. Interfaces* **2019**, *11*, 7639−7654.
(9) Foley, B. J.; Cuthriell, S.; Yazdi, S.; Chen, A. Z.; Guthrie, S. M.; Deng, X.; Giri, G.; Lee, S.; Xiao, K.; Doughty, B.; et al. Impact of Crystallographic Orientation Disorders on Electronic Heterogeneities in Metal Halide Perovskite Thin Films. *Nano Lett.* **2018**, *18*, 6271−6278.
(10) Yu, Y.; Lu, X.; Guillaussier, A.; Voggu, V. R.; Pineros, W.; de la Mata, M.; Arbiol, J.; Smilgies, D.-M.; Truskett, T. M.; Korgel, B. A. Orientationally Ordered Silicon Nanocrystal Cuboctahedra. *Nano Lett.* **2016**, *16*, 7814−7821.
(11) Harfenist, S. A.; Wang, Z. L.; Alvarez, M. M.; Vezmar, I.; Whetten, R. L. Highly Oriented Molecular Ag Nanocrystal Arrays. *J. Phys. Chem. A* **1996**, *100*, 13904−31910.
(12) Boles, M. A.; Engel, M.; Talapin, D. V. Self-Assembly of Colloidal Nanocrystals: From Intricate Structures to Functional Materials. *Chem. Rev.* **2016**, *116*, 11220−11289.
(13) Shamsi, J.; Urban, A. S.; Imran, M.; De Trizio, L.; Manna, L. Metal Halide Perovskite Nanocrystals: Synthesis, Post-Synthesis Modifications, and Their Optical Properties. *Chem. Rev.* **2019**, *119*, 3296−3348.
(14) Li, R.; Bian, K.; Hanrath, T.; Bassett, W. A.; Wang, Z. Decoding the Superlattice and Interface Structure of Truncate PbS Nanocrystal-Assembled Supercrystal and Associated Interaction Forces. *J. Am. Chem. Soc.* **2014**, *136*, 12047−12055.
(15) Huang, X.; Zhu, J.; Ge, B.; Deng, K.; Wu, X.; Xiao, T.; Jiang, T.; Quan, Z.; Cao, T. C.; Wang, Z. Understanding Fe_3O_4 Nanocube Assembly with Reconstruction of a Consistent Superlattice Phase Diagram. *J. Am. Chem. Soc.* **2019**, *141*, 3198−3206.
(16) Fan, Z.; Grunwald, M. Orientational Order in Self-Assembled Nanocrystal Superlattices. *J. Am. Chem. Soc.* **2019**, *141*, 1980−1988.
(17) Zhu, H.; Cai, T.; Que, M.; Song, J.-P.; Rubenstein, B. M.; Wang, Z.; Chen, O. Pressure-Induced Phase Transformation and Band-Gap Engineering of Formamidinium Lead Iodide Perovskite Nanocrystals. *J. Phys. Chem. Lett.* **2018**, *9*, 4199−4205.
(18) Gordon, T. R.; Diroll, B. T.; Paik, T.; Doan-Nguyen, V. V. T.; Gaulding, E. A.; Murray, C. B. Characterization of Shape and Monodispersity of Anisotropic Nanocrystals through Atomistic X-ray Scattering Simulation. *Chem. Mater.* **2015**, *27*, 2502−2506.
(19) Soetan, N.; Erwin, W. R.; Tonigan, A. M.; Walker, D. G.; Bardhan, R. Solvent-Assisted Self-Assembly of $CsPbBr_3$ Perovskite Nanocrystals into One-Dimensional Superlattice. *J. Phys. Chem. C* **2017**, *121*, 18186−18194.
(20) Huang, W.; Liu, J.; Bai, B.; Huang, L.; Xu, M.; Liu, J.; et al. Perovskite Nanocrystals: Across- Dimensional Attachment, Film-Scale Assembly on a Flexible Substrate and Their Fluorescence Properties. *Nanotechnology* **2018**, *29*, No. 125606.
(21) Becker, M. A.; Bodnarchuk, M. I.; Mahrt, R. F.; Kovalenko, M. V.; Stöferle, T. Superfluorescence from Lead Halide Perovskite Quantum Dot Superlattices. *Nature* **2018**, *563*, 671−675.
(22) Nagaoka, Y.; Hills-Kimball, K.; Tan, R.; Li, R.; Wang, Z.; Chen, O. Nanocube Superlattices of Cesium Lead Bromide Perovskites and Pressure-Induced Phase Transformations at Atomic and Mesoscale Levels. *Adv. Mater.* **2017**, *29*, No. 1606666.
(23) Tong, Y.; Yao, E.; Manzi, A.; Bladt, E.; Wang, K.; Döblinger, M.; Bals, S.; Müller-buschbaum, P.; Urban, A. S.; Polavarapu, L.; et al. Spontaneous Self-Assembly of Perovskite Nanocrystals into Electronically Coupled Supercrystals: Toward Filling the Green Gap. *Adv. Mater.* **2018**, *30*, No. 1801117.
(24) Van Der Burgt, J. S.; Geuchies, J. J.; Van Der Meer, B.; Vanrompay, H.; Zanaga, D.; Zhang, Y.; Albrecht, W.; Petukhov, A. V.; Filion, L.; Bals, S.; et al. Cuboidal Supraparticles Self-Assembled from Cubic $CsPbBr_3$ Perovskite Nanocrystals. *J. Phys. Chem. C* **2018**, *122*, 15706−15712.
(25) Kovalenko, M. V.; Bodnarchuk, M. I. Lead Halide Perovskite Nanocrystals: From Discovery to Self-Assembly and Applications. *Chimia Int. J. Chem.* **2017**, *71*, 461−470.
(26) Vovk, I. A.; Tepliakov, N. V.; Baimuratov, A. S.; Leonov, M. Y.; Baranov, A. V.; Fedorov, A. V.; Rukhlenko, I. D. Excitonic Phenomena in Perovskite Quantum-Dot Supercrystals. *Phys. Chem. Chem. Phys.* **2018**, *20*, 25023−25030.
(27) Bekenstein, Y.; Dahl, J. C.; Huang, J.; Osowiecki, W. T.; Swabeck, J. K.; Chan, E. M.; Yang, P.; Alivisatos, A. P. The Making and Breaking of Lead-Free Double Perovskite Nanocrystals of Cesium Silver-Bismuth Halide Compositions. *Nano Lett.* **2018**, *18*, 3502−3508.
(28) Vybornyi, O.; Yakunin, S.; Kovalenko, M. V. Polar-Solvent-Free Colloidal Synthesis of Highly Luminescent Alkylammonium Lead Halide Perovskite Nanocrystals. *Nanoscale* **2016**, *8*, 6278−6283.
(29) Wang, L.; Williams, N. E.; Malachosky, E. W.; Otto, J. P.; Hayes, D.; Wood, R. E.; Guyot-sionnest, P.; Engel, G. S. Scalable Ligand-Mediated Transport Synthesis of Organic−Inorganic Hybrid Perovskite Nanocrystals with Resolved Electronic Structure and Ultrafast Dynamics. *ACS Nano* **2017**, *11*, 2689−2696.
(30) Zhang, F.; Zhong, H.; Chen, C.; Wu, X.; Hu, X.; Huang, H.; et al. Brightly Luminescent and Color- Tunable Colloidal $CH_3NH_3PbX_3$ (X = Br, I, Cl) Quantum Dots: Potential Alternatives for Display Technology. *ACS Nano* **2015**, *3*, 4533−4542.
(31) Shamsi, J.; Abdelhady, A. L.; Accornero, S.; Arciniegas, M.; Goldoni, L.; et al. N-Methylformamide as a Source of Methyl-

DOI: 10.1021/acs.jpcc.9b03223
J. Phys. Chem. C 2019, 123, 17555−17565

ammonium Ions in the Synthesis of Lead Halide Perovskite Nanocrystals and Bulk Crystals. *ACS Energy Lett.* **2016**, *1*, 1042−1048.
(32) Zhang, F.; Huang, S.; Wang, P.; Chen, X.; Zhao, S.; Dong, Y.; Zhong, H. Colloidal Synthesis of Air-Stable $CH_3NH_3PbI_3$ Quantum Dots by Gaining Chemical Insight into the Solvent Effects. *Chem. Mater.* **2017**, *29*, 3793−3799.
(33) Shi, Z.-F.; Li, Y.; Li, S.; Ji, H.-F.; Lei, L.-Z.; Wu, D.; Xu, T.-T.; Xu, J.-M.; Tian, Y.-T.; Li, X.-J. Polarized Emission Effect Realized in $CH_3NH_3PbI_3$ Perovskite Nanocrystals. *J. Mater. Chem. C* **2017**, *5*, 8699−8706.
(34) Saliba, M.; Buonassisi, T.; Grätzel, M.; Abate, A.; Tress, W.; Hagfeldt, A. Promises and Challenges of Perovskite Solar Cells. *Science* **2017**, *358*, 739−744.
(35) Huang, H.; Bodnarchuk, M. I.; Kershaw, S. V.; Kovalenko, M. V.; Rogach, A. L. Lead Halide Perovskite Nanocrystals in the Research Spotlight: Stability and Defect Tolerance. *ACS Energy Lett.* **2017**, *2*, 2071−2083.
(36) Swarnkar, A.; Marshall, A. R.; Sanehira, E. M.; Chernomordik, B. D.; Moore, D. T.; Christians, J. A.; Chakrabarti, T.; Luther, J. M. Quantum Dot-Induced Phase Stabilization of α-$CsPbI_3$ Perovskite for High Efficiency Photovoltaics. *Science* **2016**, *354*, 92−95.
(37) Gualdrón-Reyes, A. F.; Yoon, S. J.; Barea, E. M.; Agouram, S.; Muñoz-Sanjosé, V.; Meléndez, ÁM.; Niño-Gómez, M. E.; Mora-Seró, I. Controlling the Phase Segregation in Mixed Halide Perovskites through Nanocrystal Size. *ACS Energy Lett.* **2019**, *4*, 54−62.
(38) Wang, X.; Ling, Y.; Lian, X.; Xin, Y.; Dhungana, K. B.; Perez-Orive, F.; Knox, J.; Chen, Z.; Zhou, Y.; Beery, D.; et al. Suppressed Phase Separation of Mixed-Halide Perovskites Confined in Endotaxial Matrices. *Nat. Commun.* **2019**, *10*, No. 695.
(39) Singh, S.; Li, C.; Panzer, F.; Narasimhan, K. L.; Graeser, A.; Gujar, T. P.; Ko, A.; Thelakkat, M.; Huettner, S.; Kabra, D. Effect of Thermal and Structural Disorder on the Electronic Structure of Hybrid Perovskite Semiconductor $CH_3NH_3PbI_3$. *J. Phys. Chem. Lett.* **2016**, *7*, 3014−3021.
(40) Weller, M. T.; Weber, O. J.; Henry, P. F.; Di Pumpo, A. M.; Hansen, T. C. Complete Structure and Cation Orientation in the Perovskite Photovoltaic Methylammonium Lead Iodide between 100 and 352 K. *Chem. Commun.* **2015**, *51*, 4180−4183.
(41) Baikie, T.; Fang, Y.; Kadro, J. M.; Schreyer, M.; Wei, F.; Mhaisalkar, S. G.; Graetzel, M.; White, T. J. Synthesis and Crystal Chemistry of the Hybrid Perovskite $(CH_3NH_3)PbI_3$ for Solid-State Sensitised Solar Cell Applications. *J. Mater. Chem. A* **2013**, *1*, 5628−5641.
(42) Stoumpos, C. C.; Malliakas, C. D.; Kanatzidis, M. G. Semiconducting Tin and Lead Iodide Perovskites with Organic Cations: Phase Transitions, High Mobilities, and near-Infrared Photoluminescent Properties. *Inorg. Chem.* **2013**, *52*, 9019−9038.
(43) Bohn, B. J.; Simon, T.; Gramlich, M.; Richter, A. F.; Polavarapu, L.; Urban, A. S.; Feldmann, J. Dephasing and Quantum Beating of Excitons in Methylammonium Lead Iodide Perovskite Nanoplatelets. *ACS Photonics* **2018**, *5*, 648−654.
(44) Huang, W.; Sadhu, S.; Ptasinska, S. Heat- and Gas-Induced Transformation in $CH_3NH_3PbI_3$ Perovskites and Its Effect on the Efficiency of Solar Cells. *Chem. Mater.* **2017**, *29*, 8478−8485.
(45) Dualeh, A.; Gao, P.; Seok, S. I.; Nazeeruddin, M. K.; Gratzel, M. Thermal Behavior of Methylammonium Lead-Trihalide Perovskite Photovoltaic Light Harvesters. *Chem. Mater.* **2014**, *26*, 6160−6164.
(46) Juarez-Perez, E. J.; Hawash, Z.; Raga, S. R.; Ono, L. K.; Qi, Y. Thermal Degradation of $CH_3NH_3PbI_3$ Perovskite into NH_3 and CH_3I Gases Observed by Coupled Thermogravimetry−mass Spectrometry Analysis. *Energy Environ. Sci.* **2016**, *9*, 3406−3410.
(47) Tan, K. W.; Moore, D. T.; Saliba, M.; Sai, H.; Estroff, L. A.; Hanrath, T.; Snaith, H. J.; Wiesner, U. Thermally Induced Structural Evolution and Performance of Mesoporous Block Copolymer-Directed Alumina Perovskite Solar Cells. *ACS Nano* **2014**, *8*, 4730−4739.
(48) Kim, N.; Min, Y. H.; Noh, S.; Cho, E.; Jeong, G.; Ahn, S.; Lee, J. S.; Kim, S.; Ihm, K.; Ahn, H.; et al. Investigation of Thermally Induced Degradation in $CH_3NH_3PbI_3$ Perovskite Solar Cells Using In-Situ Synchrotron Radiation Analysis. *Sci. Rep.* **2017**, *7*, No. 4645.
(49) Fan, Z.; Xiao, H.; William, A.; Iii, G.; Huang, Y.; Fan, Z.; Xiao, H.; Wang, Y.; Zhao, Z.; Lin, Z.; et al. Layer-by-Layer Degradation of Methylammonium Lead Tri-Iodide Perovskite Microplates. *Joule* **2017**, *1*, 548−562.
(50) Xu, R.; Li, Y.; Jin, T.; Liu, Y.; Bao, Q.; Carroll, C. O.; Tang, J. In Situ Observation of Light Illumination-Induced Degradation in Organometal Mixed-Halide Perovskite Films. *ACS Appl. Mater. Interfaces* **2018**, *10*, 6737−6746.
(51) Guillaussier, A.; Yu, Y.; Voggu, V. R.; Aigner, W.; Cabezas, C. S.; Houck, D. W.; Shah, T.; Smilgies, D. M.; Pereira, R. N.; Stutzmann, M.; et al. Silicon Nanocrystal Superlattice Nucleation and Growth. *Langmuir* **2017**, *33*, 13068−13076.
(52) Smilgies, D.; Blasini, D. R.; Smilgies, D.; Blasini, D. R. Indexation Scheme for Oriented Molecular Thin Films Studied with Grazing-Incidence Reciprocal-Space Mapping. *J. Appl. Crystallogr.* **2007**, *40*, 716−718.
(53) Shi, D.; Adinolfi, V.; Comin, R.; Yuan, M.; Alarousu, E.; Buin, A.; Chen, Y.; Hoogland, S.; Rothenberger, A.; Katsiev, K.; et al. Low Trap-State Density and Long Carrier Diffusion in Organolead Trihalide Perovskite Single Crystals. *Science* **2015**, *347*, 519−522.
(54) Hutter, E. M.; Gélvez-Rueda, M. C.; Osherov, A.; Bulović, V.; Grozema, F. C.; Stranks, S. D.; Savenije, T. J. Direct-Indirect Character of the Bandgap in Methylammonium Lead Iodide Perovskite. *Nat. Mater.* **2017**, *16*, 115−120.
(55) Choi, J. J.; Alpert, M. R.; Harper, A. F.; Smilgies, D. Controlling Nucleation, Growth, and Orientation of Metal Halide Perovskite Thin Films with Rationally Selected Additives. *J. Mater. Chem. A* **2016**, *5*, 113−123.
(56) Haruyama, J.; Sodeyama, K.; Han, L.; Tateyama, Y. Termination Dependence of Tetragonal $CH_3NH_3PbI_3$ Surfaces for Perovskite Solar Cells. *J. Phys. Chem. Lett.* **2014**, *5*, 2903−2909.
(57) Smallenburg, F.; Filion, L.; Marechal, M.; Dijkstra, M. Vacancy-Stabilized Crystalline Order in Hard Cubes. *Proc. Natl. Acad. Sci. U.S.A.* **2012**, *109*, 17886−17890.
(58) Zhang, Y.; Huang, F.; Mi, Q. Preferential Facet Growth of Methylammonium Lead Halide Single Crystals Promoted by Halide Coordination. *Chem. Lett.* **2016**, *45*, 1030−1032.
(59) Jao, M.; Lu, C.; Tai, P.; Su, W. Precise Facet Engineering of Perovskite Single Crystals by Ligand- Mediated Strategy. *Cryst. Growth Des.* **2017**, *17*, 5945−5952.
(60) Nie, W.; Tsai, H.; Asadpour, R.; Blancon, J.-C.; Neukirch, A. J.; Gupta, G.; Crochet, J. J.; Chhowalla, M.; Tretiak, S.; Alam, M. A.; et al. High-Efficiency Solution-Processed Perovskite Solar Cells with Millimeter-Scale Grains. *Science* **2015**, *347*, 522−525.
(61) Zhang, W.; Saliba, M.; Moore, D. T.; Pathak, S. K.; Hörantner, M. T.; Stergiopoulos, T.; Stranks, S. D.; Eperon, G. E.; Alexander-Webber, J. A.; Abate, A.; et al. Ultrasmooth Organic-Inorganic Perovskite Thin-Film Formation and Crystallization for Efficient Planar Heterojunction Solar Cells. *Nat. Commun.* **2015**, *6*, No. 6142.
(62) Chen, A. Z.; Foley, B. J.; Ma, J. H.; Alpert, M. R.; Niezgoda, J. S.; Choi, J. J. Crystallographic Orientation Propagation in Metal Halide Perovskite Thin Films. *J. Mater. Chem. A* **2017**, *5*, 7796−7800.
(63) Deretzis, I.; Alberti, A.; Pellegrino, G.; Smecca, E.; Giannazzo, F.; Sakai, N.; Miyasaka, T.; La Magna, A.; Deretzis, I.; Alberti, A.; et al. Atomistic Origins of $CH_3NH_3PbI_3$ Degradation to PbI_2 in Vacuum. *Appl. Phys. Lett.* **2015**, *106*, No. 131904.
(64) Xue, Y.; Shan, Y.; Xu, H.; Xue, Y.; Shan, Y.; Xu, H. First-Principles Study on the Initial Decomposition Process of $CH_3NH_3PbI_3$. *J. Chem. Phys.* **2017**, *147*, No. 124702.
(65) Alberti, A.; Deretzis, I.; Pellegrino, G.; Bongiorno, C.; Smecca, E.; Mannino, G.; Giannazzo, F.; Condorelli, G. G.; Sakai, N.; Miyasaka, T.; et al. Similar Structural Dynamics for the Degradation of $CH_3NH_3PbI_3$ in Air and in Vacuum. *ChemPhysChem* **2015**, *16*, 3064−3071.
(66) Diroll, B. T.; Guo, P.; Schaller, R. D. Unique Optical Properties of Methylammonium Lead Iodide Nanocrystals Below the Bulk

DOI: 10.1021/acs.jpcc.9b03223
J. Phys. Chem. C 2019, 123, 17555−17565

Tetragonal-Orthorhombic Phase Transition. *Nano Lett.* **2018**, *18*, 846−852.
(67) Condeles, J. F.; Ando, R. A.; Mulato, M. Optical and Structural Properties of PbI_2 Thin Films. *J. Mater. Sci.* **2008**, *43*, 525−529.
(68) Beckmann, P. A. A Review of Polytypism in Lead Iodide. *Cryst. Res. Technol.* **2010**, *460*, 455−460.
(69) Palosz, B.; Winkler, B.; Dove, M. T.; Cheng, C.; Needs, R. J.; Heine, V. In Situ Observation of the Polytypic Phase Transition 2H-12R in PbI_2: Investigations of the Thermodynamic Structural and Dielectric Properties. *J. Phys. C: Solid State Phys.* **1987**, *20*, 4077−4096.
(70) Minagawa, T. Common Polytypes of PbI_2 at Low and High Temperatures and the 2H-12R Transformation. *Acta Crystallogr., Sect. A: Cryst. Phys., Diffr., Theor. Gen. Crystallogr.* **1975**, *31*, 823−825.
(71) Zheng, Z.; Liu, A.; Wang, S.; Wang, Y.; Li, Z.; Lau, M.; Zhang, L. In Situ Growth of Epitaxial Lead Iodide Films Composed of Hexagonal Single Crystals. *J. Mater. Chem.* **2005**, *15*, 4555−4559.

DOI: 10.1021/acs.jpcc.9b03223
J. Phys. Chem. C 2019, 123, 17555−17565